Modeling solid-liquid interface reactions with next generation extended Lagrangian quantum-based molecular dynamics [†]

Kevin G. Kleiner,[‡] Aparna Nair-Kanneganti,[‡] Christian F. A. Negre,[*,¶] Ivana Matanovic,[*,§,¶] and Anders M. N. Niklasson[*,¶]

[‡]*Computational Physics division, Los Alamos National Laboratory, Los Alamos, NM 87545*
[¶]*Theoretical division, Los Alamos National Laboratory, Los Alamos, NM 87545*
[§]*Department of Chemical and Biological Engineering, Center for Micro-Engineered Materials, University of New Mexico, Albuquerque, NM 87131, USA*

E-mail: cnegre@lanl.gov; ivana@lanl.gov; amn@lanl.gov

1

Abstract

We demonstrate the applicability of extended Lagrangian Born-Oppenheimer quantum-based molecular dynamics (XL-BOMD) to model electron transfer reactions occurring on solid-liquid interfaces. Specifically, we consider the reduction of O_2 as catalyzed at the interface of an N-doped graphene sheet and H_2O at fuel cell cathodes. This system is a good testbed for next-generation computational chemistry methods since the electrochemical functionalities strongly depend on atomic-scale quantum mechanics. As opposed to prior iterations of first principles molecular dynamics, XL-BOMD only requires a full self-consistent-charge relaxation during the initial time step. The electronic ground state and total energy are stabilized thereafter through nuclear and electronic equations of motion assisted by an inner-product kernel updated with low-rank approximations. A species charge analysis reveals that the kernel-based XL-BOMD simulation can capture an electron transfer between the PGM-free catalyst and a solvated O_2 molecule mediated by H_2O, which results in the molecular dissociation of O_2.

I. Introduction

Catalyzing the O_2 reduction reaction taking place at fuel cell cathodes is paramount for the development of clean technologies that can produce electricity from molecular fuels such as hydrogen, carbon monoxide, and methanol.[1,2] Platinum-group-metals (PGM) are currently the best catalysts for the cathode O_2 reduction kinetics.[3] Unfortunately, these materials are expensive and scarce, so more economical catalytic materials for the reduction of O_2 to H_2O are necessary. One such possibility are platinum-group-metal free (PGM-free) catalysts based on metal-nitrogen-doped graphene at an interface with liquid H_2O.[4]

However, the roles of chemically active catalyst sites and solution solvents responsible for charge transfers are still under debate. Further atomic-scale modeling in more realistic fuel cell conditions is necessary prior to optimizing these catalytic materials for commercial applications.[5] Next-generation computational chemistry methods such as first principles quantum-based molecular dynamics (QMD) are essential to capture the precise inter-atomic forces and orbital structures involved in the O_2 reduction.[6] This is especially important for PGM-free catalysts since the reaction mechanisms are highly dependent on the specific geometry of the active sites and their surrounding as well as charge transfer pathways from the electrolyte.[7,8] With these accurate predictive capabilities, materials engineers can provide rational guidance for the development catalytic metallic surfaces and solutions for optimized O_2 reduction reactions.

Static first principles density functional theory (DFT) calculations provide useful and often accurate predictions for charge transfer reaction energetics and activation barriers. For instance, DFT calculations for N-doped graphene O_2 reduction catalysts predicted that O_2 adsorption becomes more energetically favorable with increasing N-sites.[9] Beyond this, it is also important to comprehensively study the charge dynamics and intermediate species involved in this process without forgoing the atomic-level electrostatic accuracy. First principles QMD simulations provide this capability since the local dynamics of the nuclear configuration and electronic structure of the system are taken into account.[10,11] For instance, this has been done for Pt(111) surface catalysts in aqueous environments.[12]

A major drawback QMD simulations based on the Born-Oppenheimer approximation is the massive overhead of calculating the electronic ground state density prior to any force evaluations during a time step.[13] Just one self-consistent field (SCF) optimization is computationally expensive since it requires repeatedly solving the Schrödinger equation for the electronic structure. In the case of catalytic solid-liquid interfaces with full solvation, SCF optimization can also be very difficult to converge due to the metallic-like electronic structure of the system, which further increases the cost

and limits the accessible time scale of a QMD simulation.[14] In this paper, we will demonstrate the potential of next generation extended Lagrangian first principles molecular dynamics (XL-BOMD) methods[11] to simulate reactive chemistry on catalytic solid-liquid interfaces without the additional overhead from iterative SCF optimization.

XL-BOMD, as formulated by Niklasson and co-workers,[11,15–20] only requires one diagonalization (or density matrix construction) during each time step prior to integrating the equations of motion for the nuclear and electronic degrees of freedom. Recently, it was shown that XL-BOMD could be improved by including an inner-product kernel operator for the electronic degrees of freedom,[11,20] such that the electron density is maintained close to the exact ground state during QMD. Various older versions of XL-BOMD have been implemented for Gaussian-based methods[15] or plane-wave pseudo potentials[21] in CONQUEST,[22,23] ONETEP,[24] and in the density-functional tight-binding (DFTB) electronic structure methods in computational packages such as LATTE[25] and DFTB+.[26] First principles QMD-DFTB has been effective for the similar problem of determining the chemical functionality of polycyclic aromatic hydrocarbons when immersed in glycine solution.[27]

In this work, we test the most recent formulation of XL-BOMD[11] with a rank-1 updated kernel in a developer test version of the LATTE program package.[25] For the specific system of an O_2 molecule at an interface with an N-doped graphene sheet and H_2O where catalyzed O_2 reduction can occur, we first verify the utility of the kernel as aiding in initial SCF convergence. We then perform femtosecond-resolved XL-BOMD simulations for several picoseconds to show consistent total energy conservation and evidence of charge transfer occurring at the solid-liquid interface.

II. Methods

Here, we will briefly present the methods used in the simulation of the catalytic solid-liquid interface. It is based on XL-BOMD, which recently was reviewed in Ref.[11] We start by defining the shadow potential energy surface, which is included in our SCF-free version of XL-BOMD. Thereafter, we present our particular formalism for density-functional tight-binding theory and how the rank-1 updated kernel works, which is a key ingredient in our formalism.

A. Shadow Potential Energy Surface

The ground state electron density ρ_{min} for an electron system in Kohn-Sham density DFT[28,29] is determined through the constrained minimization

$$\rho_{min}(\mathbf{r}) = \arg \min_{\rho \in N} \left\{ F[\rho] + \int v(\mathbf{R}, \mathbf{r})\rho(\mathbf{r})d\mathbf{r} \right\}. \quad (1)$$

Here $\mathbf{R}$ denotes a nuclear position and $\mathbf{r}$ denotes a continuum position for the density. This constrained minimization occurs over all N-representable (or v-representable) densities $\rho(\mathbf{r}) \in N$ of the universal functional $F[\rho]$ and with the external potential $v(\mathbf{R}, \mathbf{r})$. The exact minimized density ρ_{min} in Eq. (1) gives us the Born-Oppenheimer (BO) potential energy surface, $U_{BO}(\mathbf{R})$ at nuclear positions $\mathbf{R}$,

$$U_{BO}(\mathbf{R}) = F[\rho_{min}] + \int v(\mathbf{R}, \mathbf{r})\rho_{min}(\mathbf{r})d\mathbf{r} + V(\mathbf{R}), \quad (2)$$

where $V(\mathbf{R})$ is the ion-ion repulsive potential.

Determining the BO potential energy surface requires an iterative SCF optimization procedure prior to each force evaluation in a QMD simulation. The total cost of each QMD time step scales almost linearly with the number of SCF cycles, since the computational cost is dominated by each iteration of the SCF procedure. To void the expensive SCF optimization, which is caused by the non-linear universal functional, $F[\rho]$, we can construct a *linearized* functional $\mathcal{F}[\rho, n] = F[\rho] + \mathcal{O}([\rho - n]^2)$ respect

to some approximate ground-state density $n(\mathbf{r})$, where

$$\mathcal{F}[\rho, n] = F[n] + \int d\mathbf{r}(\rho[\mathbf{r}] - n[\mathbf{r}]) \left. \frac{\delta F[\rho]}{\delta \rho} \right|_{\rho = n} . \quad (3)$$

We can then use this approximate universal functional to define an approximate, although fully optimized, n-dependent ground state density,

$$\varrho[n](\mathbf{r}) = \arg \min_{\rho \in N} \left\{ \mathcal{F}[\rho] + \int v(\mathbf{R}, \mathbf{r})\rho(\mathbf{r})d\mathbf{r} \right\}. \quad (4)$$

Since $\mathcal{F}[\rho, n]$ is linearized, this minimization can be performed in a single step without any iterative SCF optimization. The optimized n-dependent ground state density, $\varrho[n](\mathbf{r})$, gives us the corresponding, approximate *shadow* Born-Oppenheimer potential energy surface,

$$\mathcal{U}_{\mathrm{BO}}(\mathbf{R}, n) = \mathcal{F}[\varrho[n], n] + \int v(\mathbf{R}, \mathbf{r})\varrho[n](\mathbf{r})d\mathbf{r} + V(\mathbf{R}). \quad (5)$$

B. Extended Lagrangian Born-Oppenheimer Molecular Dynamics

XL-BOMD, in its most recent formulation, is based on the shadow Born-Oppenheimer potential in Eq. (5), where the density, $n(\mathbf{r})$, is included as an extended dynamical field variable that evolves through a harmonic oscillator centered around the optimized ground state density, $\varrho[n](\mathbf{r})$. The extended Lagrangian is defined by

$$L(\mathbf{R}, \dot{\mathbf{R}}, n, \dot{n}) = \frac{1}{2} \sum_I M_I \dot{R}_I^2 - \mathcal{U}_{BO}(\mathbf{R}, n)$$
$$+ \frac{\mu}{2} \int \dot{n}^2(\mathbf{r})d\mathbf{r}$$
$$- \frac{\mu\omega^2}{2} \int (\varrho[n](\mathbf{r}) - n(\mathbf{r}))K(\mathbf{r}', \mathbf{r})$$
$$\times K(\mathbf{r}', \mathbf{r}'')(\varrho[n](\mathbf{r}'') - n(\mathbf{r}''))d\mathbf{r}d\mathbf{r}'d\mathbf{r}''. \quad (6)$$

where M_I denotes the nuclear mass of atom I, R_I the nuclear coordinates, $\mathcal{U}_{BO}$ the Shadow Born-Oppenheimer potential energy surface, $\varrho[n]$ the optimized ground state density based on the linearized universal functional, n the dynamical variable electron density, μ a fictitious mass parameter, and ω is the harmonic oscillator's frequency.

The equations of motion are derived from the extended Lagrangian in a classical adiabatic limit with $\omega^2/\Omega^2 \to \infty$, where Ω denotes the highest nuclear vibration frequency[20] such that $\mu\omega =$ constant. With the kernel operator $K(\mathbf{r}, \mathbf{r}')$ defined as

$$K(\mathbf{r}, \mathbf{r}') = \left(\frac{\delta \varrho[n](\mathbf{r})}{\delta n(\mathbf{r}')} - \delta(\mathbf{r} - \mathbf{r}') \right)^{-1} \quad (7)$$

it can be shown[11] that the Euler-Lagrange equations of motion in the adiabatic limit are given by

$$M_I \ddot{R}_I = - \left. \frac{\partial \mathcal{U}_{BO}(\mathbf{R}, n)}{\partial R_I} \right|_n,$$
$$\ddot{n}(\mathbf{r}) = -\omega^2 \int K(\mathbf{r}, \mathbf{r}')(\varrho[n](\mathbf{r}') - n(\mathbf{r}'))d\mathbf{r}'. \quad (8)$$

The first equation corresponds to regular Kohn-Sham Born-Oppenheimer molecular dynamics, but with the potential energy surface replaced by the shadow potential and where the partial derivatives are calculated at constant density $n(\mathbf{r})$, since $n(\mathbf{r})$ is included as a dynamical field variable. In this way, we do not rely on the Hellman-Feynman theorem that requires a fully SCF-optimized ground state density. The second equation is the harmonic oscillator, where the kernel K occurs similar to a pre-conditioner, which stabilizes the evolution of the electronic degrees of freedom. The kernel is defined as the inverse of the functional derivative, corresponding to the Jacobian of the residual function, $\varrho[n](\mathbf{r}') - n(\mathbf{r}')$. Acting on the residual, the kernel behaves like a Newton minimization step towards the exact ground state density, $\rho_{min}(\mathbf{r})$, such that $n(\mathbf{r})$ appears as if it was evolving around the exact ground state density.[11] No iterative SCF optimization is needed thanks to the linearized universal functional that defines $\varrho[n]$ and the shadow Born-Oppenheimer potential energy surface. Both $\mathbf{R}$ and $n(\mathbf{r})$ can be integrated on equal footing using symplectic or geometric integration schemes, though special care is needed for the electronic degrees of freedom.[11,30]

C. Density Functional Tight Binding Theory

Although we have outlined the continuum approach, our implementation of XL-BOMD is based on self-consistent-charge density functional tight binding (SCC-DFTB) theory.[11,31] In short, the Kohn-Sham electronic energy functional is ex-

panded to second order for density fluctuations around a set of overlapping atomic densities. The bond integrals are pre-calculated and tabulated using the Slater-Koster parameterization, and the inter-atomic electrostatic interactions are coarse grained and approximated using only monopole interactions between net Mulliken charges, $-q_I$ for each atom I. This is accomplished by mapping the continuous electronic density from Kohn-Sham DFT onto individual atoms as fractional occupation numbers. SCC-DFTB requires a prior effort for the parameterization. However, the method can then be applied for any atomic configuration and the computational cost is typically reduced by 2-3 orders of magnitude compared to first-principles electronic structure calculations often without any significant loss of accuracy.[32–34]

The Mulliken excess occupation of atom I is given by

$$q_I = \frac{1}{2} \sum_{J,\alpha,\beta} (D_{I\alpha,J\beta} S_{J\beta,I\alpha} + D_{J\beta,I\alpha} S_{I\alpha,J\beta}) - n_I^e.$$
(9)

In Eq. (9), D is the density matrix, S is the orbital overlap matrix, (I, J) are atomic indices, (α, β) are atomic orbital indices corresponding to I and J respectively, and n_I^e is the valence electron occupation of neutral atom I. The index combinations refer to specific orbitals on specific atoms.

In the SCC-DFTB formalism in the limit of one diagonalization per time step, the shadow potential energy surface corresponding to Eq. (5) is given by the minimization[31,34]

$$\mathcal{U}_{\text{BO}}(\mathbf{R}, \mathbf{n}) = \min_{D \in N} \{ 2\text{Tr}[h(D - D_0)]$$
$$+ \frac{1}{2} \sum_{I,J} (2q_I - n_I)\gamma_{IJ}n_J \} + V(\mathbf{R}).$$
(10)

over all N-representable density matrices D subject to the constraints that $\text{Tr}(DS) = N_{occ}$, the total number of occupied molecular orbitals, and idempotency, i.e. $D = DSD$. In Eq. (10), (I, J) may be the same for the on-site interactions, $\mathbf{n} = (n_1, n_2, ..., n_N)$ is a vector containing dynamical variable occupations for each atom, $\mathbf{q} = (q_1, q_2, ..., q_N)$ is a vector containing approximate ground state occupations for each atom, γ_{IJ} is the Coulomb interaction matrix that is screened to a Hubbard U for the on-site interactions, h is

the charge-independent Slater-Koster Hamiltonian matrix, and D_0 is the density matrix for the neutral and non-interacting atom configuration. Throughout the rest of this article, $\mathbf{n}$ and n_I will refer to per-atom occupations instead of the continuous electron density function from previous subsections. At finite electronic temperatures $T_e > 0$, an entropy term $T_e\mathcal{S}$ is included in the minimization defining $\mathcal{U}_{\text{BO}}$[11,31] where the electronic mean-field entropy $\mathcal{S}$ is given by

$$\mathcal{S} = -2k_B \sum_i (f_i \ln(f_i) + (1 - f_i) \ln(1 - f_i)) \quad (11)$$

summed over all Kohn-Sham molecular orbitals i at chemical potential μ where k_B is the Boltzmann factor. Each orbital has energy ϵ_i with fractional occupation number $f_i = (e^{(\epsilon_i - \mu)/(k_B T_e)} + 1)^{-1} \in [0, 1]$.

The modified equations of motion for this coarse-grained XL-BOMD method[31] are

$$M_I \ddot{R}_I = -\frac{\partial \mathcal{U}_{BO}(\mathbf{R}, \mathbf{q}[\mathbf{n}])}{\partial R_I} \bigg|_n,$$
$$\ddot{\mathbf{n}} = -\omega^2 K(\mathbf{q}[\mathbf{n}] - \mathbf{n}),$$
(12)

where the kernel is now represented as an NxN matrix

$$K = \left(\left\{ \frac{\delta \mathbf{q}[\mathbf{n}]}{\delta \mathbf{n}} \right\} - I \right)^{-1}.$$
(13)

$\{\delta \mathbf{q}[\mathbf{n}]/\delta \mathbf{n}\}$ is a set of N column vectors each having length N and containing per-atom occupation response derivatives.

The nuclear equations of motion (Eq. (12)) are integrated using a leap frog scheme with time step δt. As such, the simulation can update all the nuclear positions and velocities as

$$\dot{\mathbf{R}}(t + \delta t/2) = \dot{\mathbf{R}}(t) + (\delta t/2)\ddot{\mathbf{R}}(t)$$
$$\mathbf{R}(t + \delta t) = \mathbf{R}(t) + \delta t\dot{\mathbf{R}}(t + \delta t/2)$$
$$\dot{\mathbf{R}}(t + \delta t) = \dot{\mathbf{R}}(t + \delta t/2) + (\delta t/2)\ddot{\mathbf{R}}(t + \delta t) \quad (14)$$

with initial conditions $\mathbf{R}(t_0) = \mathbf{R}_0$ and $\dot{\mathbf{R}}(t_0) = \dot{\mathbf{R}}_0$. However, if the electronic degrees of freedom in Eq. (12) were updated using the same leapfrog scheme or any other time-reversible integration scheme, they would gradually diverge from the electronic

ground state as governed by the dynamical nuclear configuration in Eq. (14).[11] This divergence is caused by an accumulation of numerical errors that accumulate within a perfectly time-reversible scheme. In terms of the O_2 reduction reaction simulation, where an integration time step is typically less than a femtosecond, and an electron transfer reaction may only occur after a few picoseconds, this systematic error accumulation magnifies uncertainties in the long run. A solution is to introduce a weak dissipation to the electronic structure updates, which can be achieved through a modified Verlet integration scheme.[30,35] This scheme includes Langevin-like noise-dissipation terms of higher order in the integration time step and can be described as a modified Verlet scheme, i.e.

$$\mathbf{n}(t + \delta t) = 2\mathbf{n}(t) - \mathbf{n}(t - \delta t)$$
$$+ \delta t^2 \ddot{\mathbf{n}}(t) + \alpha \sum_{k=0}^{k_{max}} c_k \mathbf{n}(t - k\delta t) \qquad (15)$$

with initial conditions typically chosen as $\mathbf{n}(t_0) = \mathbf{q}_{\min}(t_0)$ and $\dot{\mathbf{n}}(t_0) = \mathbf{0}$ after the initial electronic optimization of $\mathbf{q}_{\min}(t_0)$. The number of terms k_{max} of the damping term above, and the coefficients α and $\{c_k\}$ are optimized with respect to the dissipation under certain stability conditions.[11,30,35]

D. Rank-1 Kernel Approximation

The calculation of $\ddot{\mathbf{n}}$, which is driven by the harmonic oscillator, requires an update of the kernel K in each time step during a QMD simulation. This is expensive since Eq. (13) involves quantum response calculations for every atom followed by a full matrix inversion. However, in many cases, we can approximate the kernel K by a constant scaled delta function, i.e. $K = cI$. Unfortunately, this approximation is typically not sufficiently stable for the reactive chemical systems of interest in this article. Instead, we will use an approximation based on a rank-1 update of the scaled delta-function approximation in combination with fractional occupation numbers of the electronic states.[11] This technique overcomes previous stability problems and allows for efficient simulations even of reactive chemical systems without relying on any costly, iterative SCF optimization scheme.

Our method is based on a reformulation of the exact kernel defined in Eq. (13). Starting with an approximate kernel

$$K_0 = [J_0 - I]^{-1}, \qquad (16)$$

where $J_0 = cI$ with $c \neq 1$, we construct a set of orthogonal perturbation vectors $\{\mathbf{v}_i\}$, one for each rank-1 update. We can then update the approximate kernel, K_0, in the same way as we could update the columns, one by one, of the kernel defined in Eq. (13), but now along an arbitrary set of orthonormal directions $\{\mathbf{v}_i\}$. This scheme[11] (for $i = 1, 2, \ldots, N$) is given by

$$\mathbf{u}_i = \frac{\delta \mathbf{q}[\mathbf{n} + \lambda \mathbf{v}_i]}{\delta \lambda}\bigg|_{\lambda=0} - J_{i-1}\mathbf{v}_i$$

$$J_i = J_{i-1} + \mathbf{u}_i \mathbf{v}_i^T$$

$$K_i = (K_{i-1} + \mathbf{u}_i \mathbf{v}_i^T)^{-1}$$

$$= K_{i-1} - \frac{K_{i-1}\mathbf{u}_i \mathbf{v}_i^T K_{i-1}}{1 + \mathbf{v}_i^T K_{i-1} \mathbf{u}_i},$$

which involves the Sherman-Morrison formula for the inverse of a rank-1 updated matrix.[36] For a system with N atoms, the exact kernel is given after N rank-1 updates, each requiring a quantum response calculation along the directional perturbations $\delta \mathbf{q}/\delta \lambda$.[37] However, to avoid the full cost of N response calculations we can use a low-rank approximation. In our case, we use only a single rank-1 updated kernel, where we chose the $\mathbf{v}_1$ perturbation vector as

$$\mathbf{v}_1 = \frac{\mathbf{q}[\mathbf{n}] - \mathbf{n}}{||\mathbf{q}[\mathbf{n}] - \mathbf{n}||} \qquad (17)$$

such that $\mathbf{v}_1^T K_0$ becomes parallel to $\mathbf{q}[\mathbf{n}] - \mathbf{n}$. This choice gives the largest impact of K_1 when acting on the residual $\mathbf{q}[\mathbf{n}] - \mathbf{n}$ in Eq. (12).

The rank-1 updated kernels can also be applied in the initial SCF optimization required in the very first QMD time step. Niklasson[11] compared some related optimization schemes to relax the electronic structure of a hydroquinone radical immersed in H_2O, including linear mixing, Anderson/Pulay mixing,[38,39] with the rank-1 kernel updates and full kernel updates above. The full kernel updates take the fewest iterations to converge for that system. When checking this result for our model system of one O_2 molecule at an interface with a 128-atom graphene sheet (4 atoms being N dopants) and 164 H_2O molecules, we verified that

while the full kernel updates take the fewest iterations to converge, the rank-1 kernel updates provide a better compromise with respects to computing time.

IV. Constant of Motion

In the adiabatic limit where $\omega \to \infty$ and $\mu \to 0$, the constant of motion for XL-BOMD is given by the Born-Oppenheimer shadow Hamiltonian,[11]

$$\mathcal{H}_{XBO} = \frac{1}{2} \sum_I M_I \dot{R}_I^2 + \mathcal{U}_{BO}(\mathbf{R}, \mathbf{q}[\mathbf{n}]), \qquad (18)$$

which closely follows the exact Born-Oppenheimer Hamiltonian with a leading error of $\mathcal{O}([\mathbf{q}[\mathbf{n}] - \mathbf{n}]^2)$ arising from the linearization of $\mathcal{F}$ in Eq. (4). It is possible to show that the residual $(\mathbf{q}[\mathbf{n}] - \mathbf{n})$ scales quadratically with the integration time step for the modified Verlet integration scheme. In this case the leading error of the shadow Hamiltonian is only of fourth order, $\sim \delta t^4$, and in practice is virtually indistinguishable from the exact regular Born-Oppenheimer simulation.[11,31] Thus, XL-BOMD closely follows the exact Hamiltonian by maintaining the charge distribution $\mathbf{n}$ near the exact, fully optimized ground state.

The equations of motion includes both the nuclear and the electronic degrees of freedom. With a perfectly time-reversible integration scheme, any numerical noise will accumulate and never disappear. This may lead to a divergence between the electronic degrees of freedom and the corresponding nuclear coordinates, $\mathbf{R}$, such that $\mathbf{n}$ no longer follows the exact ground state charge distribution determined by $\mathbf{R}$. This may eventually lead to a breakdown of the simulation. The noise accumulation problem is demonstrated in Figure 1 using the rank-1 updated kernel approximation for the sample system of a 128-atom N-doped graphene surrounded by an O_2 molecule and 164 H_2O molecules when no noise dissipation is included, i.e. $\alpha = 0$ in Eq. (15). The QMD simulation in Figure 1 tracks the total energy deviation from an average (taken over the first 500.00 fs), where the dissipative last term in Eq. (15) is ignored. In this case the integration scheme is perfectly time-reversible.
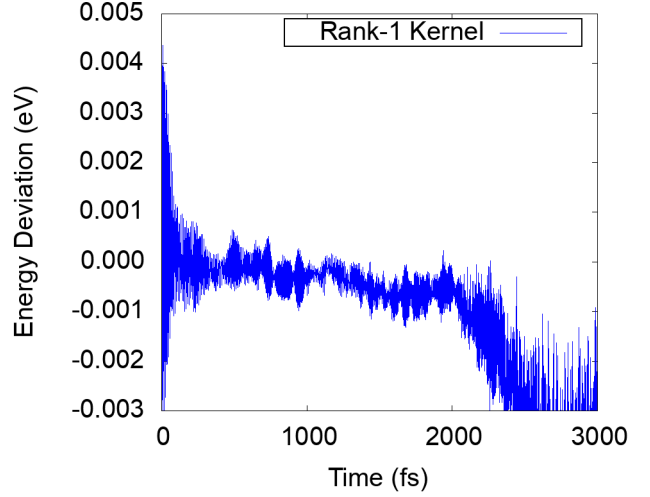

Figure 1: Total energy deviation plots during 3 ps (3000.00 fs) of QMD with periodic boundary conditions for the N-doped graphene sheet surrounded by O_2 and water using a perfectly time-reversible integration scheme both for the nuclear and electronic degrees of freedom. The kernel is updated only once every time step using the rank-1 approximation and the integration time step is 0.25 fs.

However, the total energy is unstable and breaks down after a few picoseconds of QMD simulation because of the accumulation of the numerical noise in the perfectly time-reversible integration. To counteract the noise accumulation, the modified Verlet integration scheme in Eq. (15) is used including its weak electronic dissipation term, i.e. $\alpha > 0$. The result is shown in Figure 2 with $k_{max} = 5$ using the coefficients specified in the caption. This long-term conservation of the total energy, demonstrated in Figure 2, is a sensitive gauge of the quality of a molecular dynamics simulation.
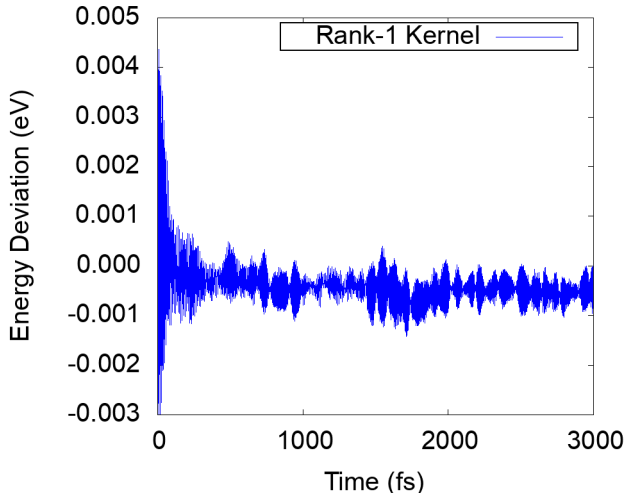
Figure 2: Total energy deviation for N-doped graphene sheet using the modified Verlet integration scheme with $\alpha = 0.018$, $\delta t^2 \omega^2 = 1.82$, and six density noise dissipation terms for calculating $n(t + \delta t)$: $c_0 = -6$, $c_1 = 14$, $c_2 = -8$, $c_3 = -3$, $c_4 = 4$, $c_5 = -1$.

V. Simulating Catalytic Interface Reactions

The XL-BOMD simulation scheme using the rank-1 updated kernel approximation and the modified Verlet integration scheme is now applied for a 10 ps time interval to simulate the N-doped graphene sheet with an O_2 molecule surrounded by 164 H_2O molecules. One possible way to identify the occurrence of the reaction is to track the HOMO-LUMO gap, the energy difference between the highest occupied molecular orbital (HOMO) and lowest unoccupied molecular orbital (LUMO), using the fact that $Tr(DS) = N_{occ}$ is held constant for the system. This gap is shown in Figure 3.
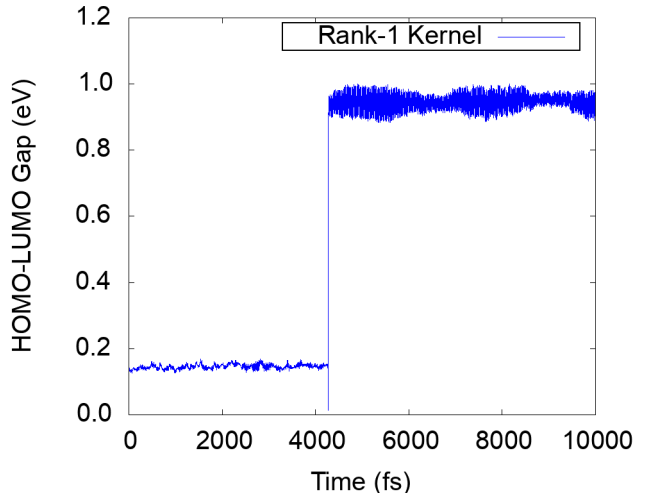

Figure 3: HOMO-LUMO gap for the system of N-doped graphene with oxygen and water over 10 ps.

This energy gap starts out with a relatively small value and suddenly changes to a relatively larger value. In a 10.00 fs interval of around 4267.00 fs to 4277.00 fs, the 0.17 eV gap size drops to nearly 0.00 eV and then grows sharply to a value of about 0.95 eV. This indicates the existence of species with higher chemical reactivity transitioning into different species with lower reactivity.[40]

Further analysis is necessary to determine exactly how the charge gets redistributed and which atomic species are involved. Therefore, a relevant subset of the configurations of the trajectory is illustrated using Visual Molecular Dynamics (VMD) software[41] before and after the HOMO-LUMO energy gap transition to understand the nature of the reactants and products.
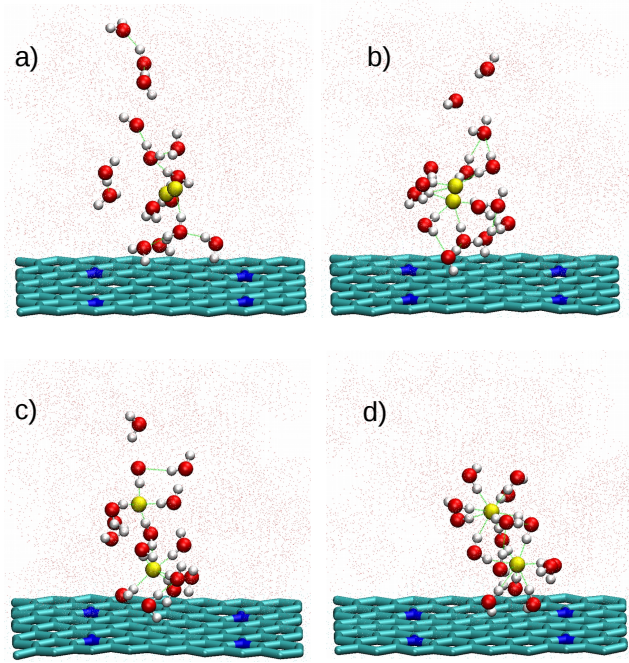
Figure 4: Molecular representation showing the system's configuration at QMD times of (a) 0.00 fs, (b) 3512.50 fs, (c) 4750.00 fs, and (d) 10412.50 fs. C, N, H, and O atoms are depicted in cyan, blue, white, and red colors respectively. The oxygen molecule is depicted in yellow. The system is inside a box of dimensions 19.686 Å x 17.048 Å x 20.000 Å with periodic boundary conditions. For clarity, only 14 of the 164 water water molecules are shown.

Figure 4 (a) and (b) depict the O_2 molecule and nearest neighboring water molecules prior to the reaction. In snapshot (b), these water molecules interact with the O_2 molecule through dipole-dipole interactions. Snapshots (c) and (d) are taken right after and long after the reaction respectively. The post-reaction configurations suggest isolated O^- ions are solvated by water. This QMD trajectory thus shows that the reaction involves breaking of the O-O (oxygen-oxygen) covalent bond. This bond-breaking is further demonstrated in Figure 5 that displays the O-O separation distance during the entire 10000.00 fs simulation time frame.
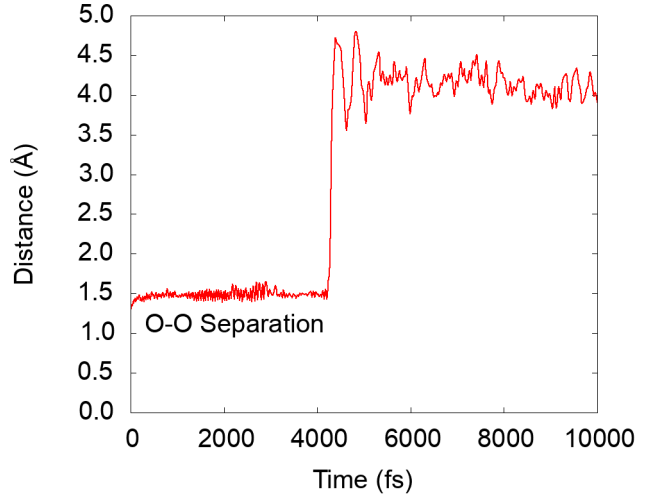

Figure 5: O-O bond distance as a function of time for a 10000.00 fs QMD simulation computed every 12.50 fs.

According to Figure 5, at the beginning of the simulation, the O_2 molecule with bond length 1.21 Å gradually increases its atomic separation to 1.50 Å. After the dissociation later, the O-O separation abruptly increases to 4.00 Å due to the hydrogen bonding from the local H_2O molecules apparent in Figure 4.

To verify that a charge transfer mechanism was involved, Figure 6 depicts the net Mulliken charges in units of the elementary charge e for every component of the system. This is calculated as $-\sum_I q_I$ using Eq. (9) for all atoms I constituting a given component. We observe that charge equivalent to one electron is transferred to the O_2 molecule from the N-doped graphene and surrounding water solvent. Specifically, the net charge of the sheet and water molecules increases during the reaction accompanied by the decrease in the charge of O_2. Note that the charges at time $t = 0$ represent the static electronic ground state resulting from initial kernel-assisted SCF optimization.
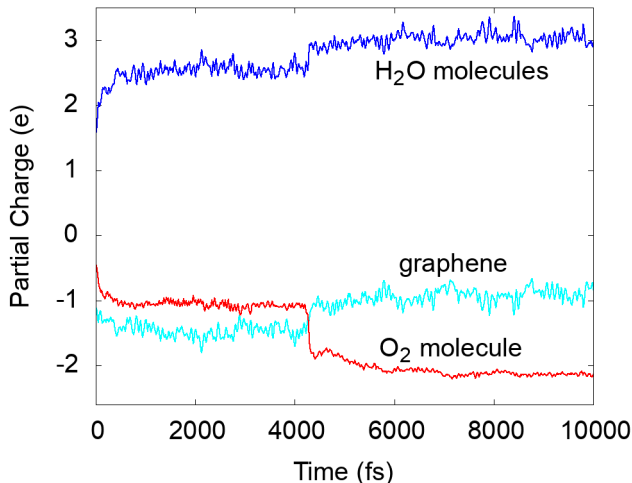
9

Figure 6: Net charges for every component of the system: N-doped graphene sheet (light blue), O_2 molecule (red), and water molecules (blue). Total simulation time is 10000.00 fs and total charges are computed every 12.50 fs.

During the dissociation, both O_2 atoms were approximately 8.00 Å above the sheet, implying that the charge transfer from the sheet to the O_2 molecule occurred indirectly. This can be explained by water molecules forming a conducting bridge between the graphene and O_2.[42] This hypothesis is supported by Figure 4 (b) where a hydrogen bonded water chain bridges the sheet and O_2 immediately prior to the reaction. By examining the charge transfer in Figure 6, the O_2 molecule acquires charge during both initial electronic relaxation and first 200.00 fs of QMD leading to the formation of a O_2^- that stays stable from 200.00 fs to 4000.00 fs. This first step alone demonstrates a single-electron reduction. After the 4272.00 fs mark, the product is $2O^-$. This dissociation reaction is indicated through the sudden change in the HOMO-LUMO energy gap to a more stable value in Figure 3. At the moment of the reaction, the HOMO-LUMO gap is reduced to zero, allowing the system to have a metallic behavior, which in turn facilitates the electron transfer. This pure H_2O dissociation near the graphene surface has been shown to not be the case with a Pt catalytic surface.[3]

Viewed in terms of the O_2 reduction mechanism, this preliminary result may provide evidence for the outer-sphere reduction.[43] In this case, the proximity of O_2 to the donor graphene surface is not required, and the charge is transferred through the H_2O comprising the solvation shell of O_2. The

molecular visualization in Figure 4 (b) shows such a shell. The full O_2 reduction reaction would require the addition of H^+ into the system, which would be the next step for this XL-BOMD method.

Broadly speaking, demonstrating the realistic charge dynamics of these species in the specific catalytic system configuration is a remarkable milestone for this next generation XL-BOMD. Static DFT could provide the most favorable product species and respective charges for this reaction, but the computationally feasible time evolution is possible due to the kernel-assisted equations of motion for both the atomic nuclei and coarse-grained electronic structure. In the light of these preliminary results for the O_2 reduction on PGM-free catalyst, we strongly believe that this method will become an important tool to simulating charge-transfer reaction chemistry at solid-liquid interfaces.

VI. Conclusions

In this article, we successfully demonstrated the ability of the next-generation XL-BOMD computational chemistry method to simulate a catalyzed O_2 reduction reaction at the interface of N-doped graphene and H_2O. This method is based on DFTB theory yielding nuclear and electronic equations of motion (integrated with a modified Verlet scheme) assisted by a rank-1 updated kernel. Our example further demonstrates that it is possible to simulate reactive chemical dynamics using modern QMD schemes without the computational challenge of previously required SCF electronic optimizations prior to each force evaluation. This significantly extends the accessible time scale of QMD simulations for more challenging reactive chemical systems, while maintaining the first principles accuracy of inter-atomic forces and ground state charge distributions.

As shown, this kernel-assisted XL-BOMD can provide useful insight into the mechanistic of geometry and solution-dependent electrocatalytic reactions beyond the energetic predictions of DFT alone. By tracking the system's HOMO-LUMO energy gap and atomic neighbors in visualizations, we were able to depict the exact starting point of the molecular dissociation part of the O_2 reduction. Moreover, we observe the outer-sphere reduction mechanism demonstrating the important role sol-

vent molecules play in the electron transfer process.

Future work should explore the role of H^+ or OH^- concentrations in the solvent as they relate to charge transfer mechanisms and bond breaking/formation resulting in O_2 reduction. By tracking the specific molecular orbitals involved, alternative reaction pathways can be identified including the formation of H_2O_2 or OH^- intermediates. For a more realistic study, next-generation QMD could involve simulations with larger graphene sheets (exceeding the 128-atom size in this paper) and multiple layers. Also, sheet defects with varying reactivates can be studied to learn about their role in the O_2 reduction mechanism. Clear understanding of the structure-function relations in these chemically reactive catalytic systems can ultimately lead to the increased efficiency of the fuel cells based on the use of PGM-free materials. By gauging the effectiveness of these fuel cell reduction catalysts as an alternative to platinum-group-metals, the cost efficiency and current production can be greatly improved.

In conclusion, we believe the next generation first principles extended Lagrangian QMD method with rank-1 approximate kernels can be used to efficiently simulate the complex charge dynamics of O_2 reduction at solid-liquid interfaces as well as other similar problems in computational chemistry.

Acknowledgements

References

(1) Morozan, A.; Jousselme, B.; Palacin, S. *Energy Environ. Sci.* **2011**, *4*, 1238–1254.

(2) Matanovic, I.; Artyushkova, K.; Atanassov, P. *Curr. Opin. Electrochem.* **2018**, *9*, 137–144.

(3) Song, C.; Zhang, J. In *PEM Fuel Cell Electrocatalysts and Catalyst Layers: Fundamentals and Applications*; Zhang, J., Ed.; Springer London: London, 2008; pp 89–134.

(4) Reyimjan, A. S.; Alfred, B. A.; Nalini, P. S.; Swaminatha, P. K.; Branko, N. P. *J. Phys. Chem. B.* **2006**, *110*, 1787–1793.

(5) Jiao, Y.; Zheng, Y.; Jaroniec, M.; Qiao, S. Z. *J. Am. Chem. Soc.* **2014**, *136*, 4394–4403.

(6) Vidossich, P.; Lledós, A.; Ujaque, G. *Acc. Chem. Res.* **2016**, *49*, 1271–1278.

(7) Ikeda, T.; Boero, M.; Huan, S.-F.; Terakura, K.; Oshima, M.; Ozaki, J.-I. *Phys. Stat. Sol.* **2008**, *112*, 14706–14709.

(8) Holby, E. F.; Zelenay, P. *Nanoen.* **2016**, *29*, 54–64.

(9) Okamoto, Y. *Appl. Surf. Sci.* **2009**, *256*, 335–341.

(10) Grotendorst, J. *Modern Methods and Algorithms of Quantum Chemistry*, 2nd ed.; NIC-Directors: Forschungszentrum Julich, Germany, 2000.

(11) Niklasson, A. M. N. *J. Chem. Phys.* **2017**, *147*, 1–5.

(12) He, Y.; Chen, C.; Yu, H.; Lu, G. *Catal. Commun.* **2016**, *87*, 74–77.

(13) Rabuck, A. D.; Scuseria, G. E. *J. Chem. Phys.* **1999**, *110*, 695–696.

(14) Kudin, K. N.; Scuseria, G. E. *Phys. Rev. Lett.* **2002**, *116*, 8255–8256.

(15) Niklasson, A. M. N. *Phys. Rev. Lett.* **2008**, *100*, 123004.

(16) Niklasson, A. M. N.; Tymczak, C. J.; Challacombe, M. *Phys. Rev. Lett.* **2006**, *97*, 123001.

(17) Cawkwell, M. J.; Niklasson, A. M. N. *J. Chem. Phys.* **2012**, *137*, 134105.

(18) Souvatzis, P.; Niklasson, A. M. N. *J. Chem. Phys.* **2013**, *139*, 214102.

(19) Negre, C. F. A.; Mniszewski, S. M.; Cawkwell, M. J.; Bock, N.; Wall, M. E.; Niklasson, A. M. N. *J. Chem. Theory Comput.* **2016**, *12*, 3063–3073.

(20) Niklasson, A. M. N.; Cawkwell, M. J. *J. Chem. Phys.* **2014**, *141*, 1–5.

(21) Steneteg, P.; Abrikosov, I. A.; Weber, V.; Niklasson, A. M. N. *Phys. Rev. B* **2010**, *82*, 075110.

(22) Arita, M.; Bowler, D. R.; Miyazaki, T. *J. Chem. Theory Comput.* **2014**, *10*, 5419–5425.

(23) Hirakawa, T.; Suzuki, T.; Bowler, D. R.; Miyazaki, T. *J. Chem. Phys.* **2017**, *29*, 1–9.

(24) Vitale, V.; Dziedzic, J.; Albaugh, A.; Niklasson, A. M. N.; Head-Gordon, T.; Skylaris, C.-K. *J. Chem. Phys.* **2017**, *146*, 124115.

(25) Bock, N.; Cawkwell, M. J.; Coe, J. D.; Krishnapriyan, A.; Kroonblawd, M. P.; Lang, A.; Liu, C.; Martinez Saez, E.; Mniszewski, S. M.; Negre, C. F. A.; Niklasson, A. M. N.; Sanville, E.; Wood, M. A.; Yang, P. LATTE. 2008; https://github.com/lanl/LATTE.

(26) Aradi, B.; Hourahine, B.; Frauenheim, T. *J. Phys. Chem. A* **2007**, *111*, 5678–5684, PMID: 17567110.

(27) Kroonblawd, M. P.; Rebecca K. Lindsey, R. K.; Nir Goldman, N. *Chem. Sci.* **2019**, *10*, 6091–6098.

(28) Parr, R. G. Density Functional Theory of Atoms and Molecules. 1980.

(29) Hohenberg, P.; Kohn, W. *Phys. Rev.* **1964**, *136*, B864–B870.

(30) Niklasson, A. M. N.; Steneteg, P.; Odell, A.; Bock, N.; Challacombe, M.; Tymczak, C. J.; Holmström, E.; Zheng, G.; Weber, V. *J. Chem. Phys.* **2009**, *130*, 214109.

(31) Aradi, B.; Niklasson, A. M. N.; Frauenheim, T. *J. Chem. Theory Comput.* **2015**, *11*, 3357–3363.

(32) Cui, Q.; Elstner, M.; Kaxiras, E.; Frauenheim, T.; Karplus, M. *J. Phys. Chem. B* **2000**, *105*, 569–585.

(33) Elstner, M.; Jalkanen, K. J.; Knapp-Mohammady, M.; Frauenheim, T.; Suhai, S. *J. Phys. Chem. B* **2001**, *263*, 203–219.

(34) Krishnapriyan, A.; Yang, P.; Niklasson, A. M. N.; Cawkwell, M. J. *J. Chem. Theory Comput.* **2017**, *13*, 6191–6200.

(35) Zheng, G.; Niklasson, A. M. N.; Karplus, M. *J. Chem. Phys.* **2011**, *135*, 044122.

(36) Sherman, J.; Morrison, W. J. *Ann. Math. Stat.* **1950**, *21*, 124–127.

(37) Niklasson, A. M. N.; Cawkwell, M. J.; Rubensson, E. H.; Rudberg, E. *Phys. Rev. E.* **2015**, *92*, 1–2.

(38) Pulay, P. *Chem. Phys. Lett.* **1980**, *73*, 393–398.

(39) Pulay, P. *J. Comput. Chem.* **1982**, *3*, 556–560.

(40) Bredas, J.-L. *Mat. Horiz.* **2014**, *1*, 17–19.

(41) Humphrey, W.; Dalke, A.; Schulten, K. *J. Molec. Graphics.* **1996**, *14*, 33–38.

(42) Negre, C. F. A.; Jara, G. E.; Vera, D. M. A.; Pierini, A. B.; Sánchez, C. G. *J. Phys.: Condens. Matter* **2011**, *23*, 245305.

(43) Ramaswamy, N.; Mukerjee, S. *J. Phys. Chem. C.* **2001**, *115*, 18015–18026.